Renewable Energy 256 (2026) 123894

Contents lists available at ScienceDirect

Renewable Energy

journal homepage: www.elsevier.com/locate/renene

Microseisms as a renewable energy resource: Nature of ubiquitous, unrelenting, and coherent ground vibrations and energy flow

Seongjun Park, Tae-Kyung Hong *

Yonsei University, Department of Earth System Sciences, 50 Yonsei-ro, Seodaemun-gu Seoul 03722, South Korea

ARTICLE INFO

Keywords:
Microseisms
Ground motion
Spatiotemporal distribution
Source inversion
Energy resource
Ocean and solid earth interaction

ABSTRACT

Unrelenting coherent ground vibrations may serve as a potential renewable energy resource. Microseisms are ubiquitous ground motions that are excited by the coupling between the solid earth and ocean waves. The continuous unrelenting energy has been limitedly utilized due to poor understanding of constitutive energy sources. We explore the high-resolution spatiotemporal distribution of microseism sources for Rayleigh waves in a frequency band of 0.225–0.275 Hz in four seasons of 2021–2022 using a novel source-strength inversion method based on a dense seismic network in the Korean Peninsula, offering an unprecedented chance for in-depth investigation of microseism nature and its potential utilization. The study identifies that the microseisms develop from a set of stationary individual offshore sources near the coasts in optimal environments, challenging the traditional view of temporally migrating sources. Multiple stationary sources with temporally-varying strengths develop a complex and coherent microseism field. These features make microseisms to produce ubiquitous, unrelenting, and coherent ground motions for a natural energy resource.

1. Introduction

Many renewable energy sources suffer from intermittency and environmental constraints, highlighting the need for more persistent and broadly applicable alternatives as complementary solutions. The solid Earth responds dynamically to various natural and anthropogenic phenomena, exciting seismic ground motions. A wide range of events, such as earthquakes [1,2], volcanic activity [3], thunder [4], traffic [5], and construction [6], may induce the ground vibrations. Coherent ground motions may be used for renewable energy applications [7,8].

Earthquakes have been considered as a potential energy source. Previous efforts to utilize seismic ground motions focused to develop energy-harvesting technology [7,8]. However, unpredictable and transient natures of earthquakes pose challenges for sustainable energy collection, limiting their practical utilization. On the other hand, microseisms may offer a persistent and stable energy source [9,10]. However, the nature of microseisms has been poorly understood, which makes it hard to consider the microseisms as a potential energy resource.

Microseisms are a major component that constitutes the ambient seismic noise at frequencies of ~0.05–0.5 Hz. The microseisms are excited by dynamic coupling between the atmosphere, ocean, and solid earth. Surface winds over the seas induce ocean waves that exert pressure at the seafloor, exciting the microseisms [11,12]. Progressive ocean waves excite microseisms at frequencies of ~0.05–0.1 Hz (primary microseisms) [9,13]. Also, standing ocean waves excite microseisms at frequencies of ~0.1–0.5 Hz (secondary microseisms) [11,14].

The microseism excitation is controlled by various factors including coastal geometry [14,15], ocean depth [12,16], seafloor topography [9,13] and medium properties [12,16]. Shallow ocean depths with uphill seafloor slopes may provide a favorable environment for microseism excitation [13,17]. However, the nature of microseism source development, temporal evolution, and source regions are not fully understood.

The microseisms are ubiquitous in the Earth [18,19]. There have been attempts to utilize microseisms for atmosphere and climate monitoring [18,20], storm tracking [21,22], ambient-noise seismic tomography [23,24], and instant determination of seismic sensor orientations [10,25]. However, the continuous unrelenting microseism energy is limitedly utilized as a potential energy resource, which is partly due to poor understanding of constitutive energy sources.

There were efforts to study the microseism source properties using regional [26,27] or teleseismic records [28,29] based on a single-source assumption, suffering from limited spatial resolution on multiple sources. Traditional studies suggest that microseism fields are dominated by single sources [30,31]. Also, it is often suggested that microseism sources are transient and migrate over time [19,21]. However, localized stationary microseism sources are observed [32]. Further,

* Corresponding author.
E-mail address: tkhong@yonsei.ac.kr (T.-K. Hong).

https://doi.org/10.1016/j.renene.2025.123894
Received 25 January 2025; Received in revised form 27 June 2025; Accepted 28 June 2025
Available online 9 July 2025

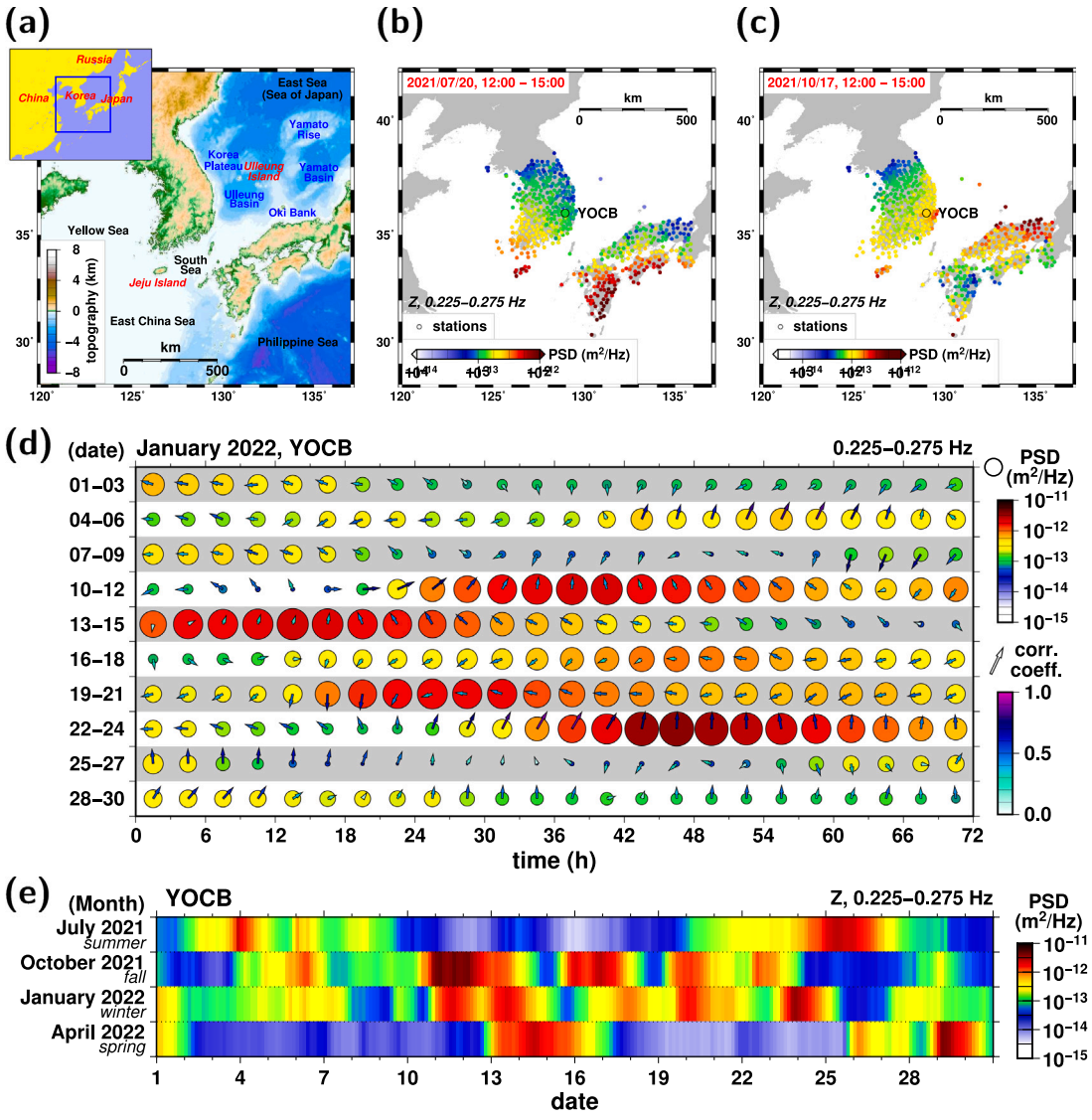

Fig. 1. (a) Map of the Korean Peninsula, southern Japanese islands and adjacent regions. Jeju Island, Ulleung Island, and major oceanic geological provinces in the East Sea (Sea of Japan) are indicated. A large map is presented (inset). Power spectral densities (PSDs) of ambient vertical ground motions at frequencies of 0.225–0.275 Hz in (b) 12:00–15:00, July 20, 2021 and (c) 12:00–15:00, October 17, 2021. Station YOCB is marked. The microseism energy exhibits substantial spatiotemporal variations. (d) Temporal changes in microseism properties at station YOCB in January 2022. The power spectral density of vertical ground motion (circles) and apparent Rayleigh-wave radial direction (arrows) for microseisms in every 3 h are presented. The correlation coefficients between the radial and 90°-phase-shifted-vertical ground motions are indicated. The strength and polarization of microseisms change over time. (e) Temporal variations in microseism amplitudes at station YOCB in four seasons. The observed microseism magnitude changes by season.

possible presence of synchronous multiple individual sources has not been adequately examined. The controversial views on microseism sources hamper the use of microseism energy.

This study investigates the spatiotemporal properties of microseism sources and induced ground motions, examining the potential of microseisms as a renewable energy resource. Seismic stations are densely deployed in the Korean Peninsula and southwestern Japanese islands that are surrounded by oceans (Fig. S1 in supplementary materials). The unique environments set up a natural laboratory to study the microseism field and source properties. We introduce a source-strength inversion method based on a dense seismic network to illuminate small-scale microseism source distribution, effective source regions, microseism source strengths, and temporal evolution. Also, we investigate the transient ground motions and polarization directions of energy flux from microseism sources, examining the possible utilization of energy flux.

2. Methods

2.1. Rayleigh-wave polarization analysis

The microseisms are mainly composed of Rayleigh-wave and Love-wave energy with fractional body-wave energy [33,34]. The polarization directions of the Rayleigh waves are perpendicular to those of the Love waves, which enables us to separate the Rayleigh waves from the Love waves in microseisms [32,35]. The retrograde elliptical particle motions of the Rayleigh waves are confined in the vertical and radial components with a 90° phase difference [32,36].

We determine the apparent radial direction of the Rayleigh waves in microseisms at a station by searching for the direction where the radial waveform is most strongly correlated with the 90°-phase-shifted vertical waveform using a time-domain correlation analysis [32,36].

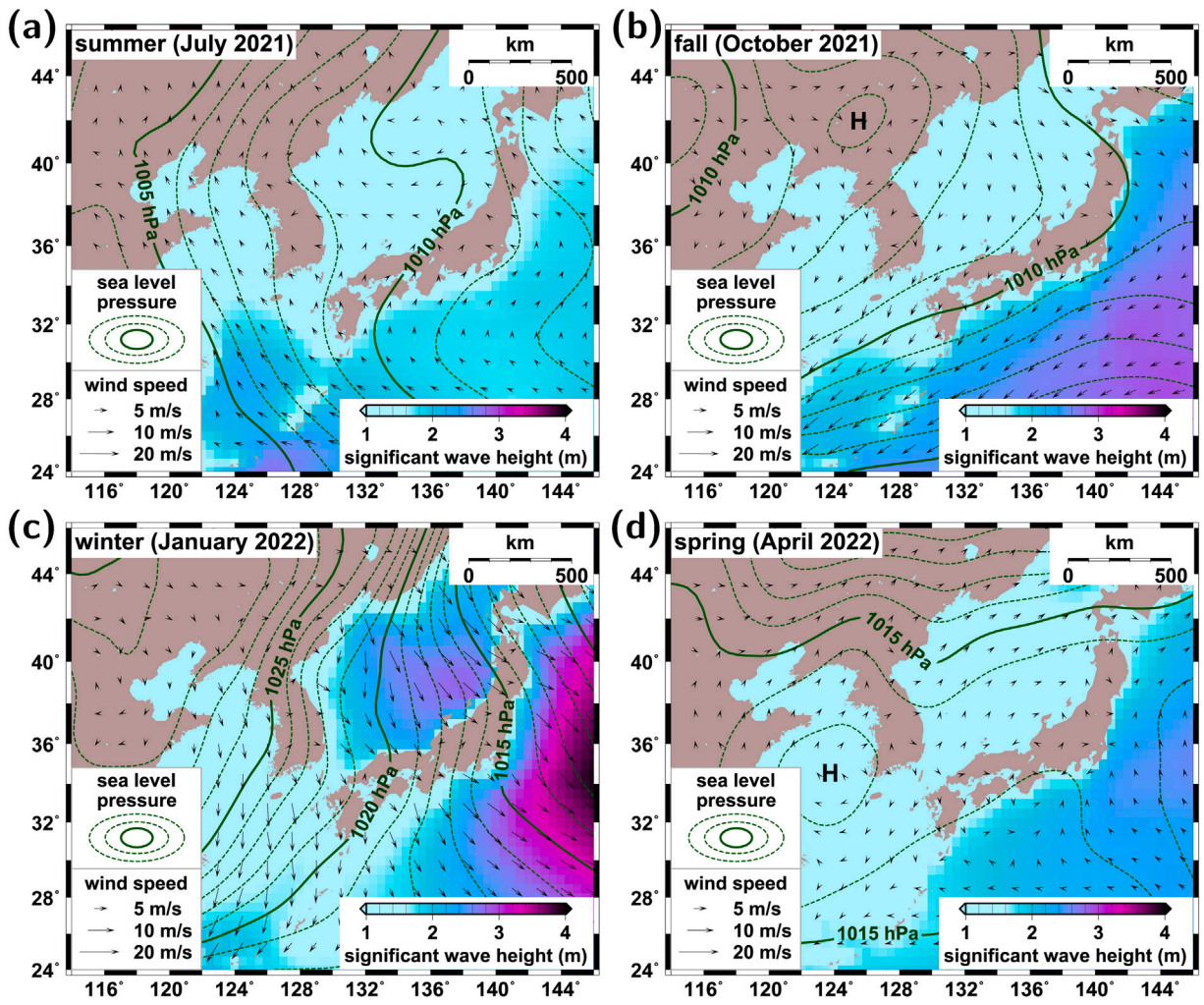

Fig. 2. Seasonal variations in atmospheric and oceanic activity. Distributions of monthly-average significant ocean-wave heights, sea-level atmospheric pressures (contour lines), and surface wind fields (arrows) around the Korean Peninsula in (a) the summer of 2021 (July 2021), (b) fall of 2021 (October 2021), (c) winter of 2022 (January 2022), and (d) spring of 2022 (April 2022) are presented. The atmospheric and oceanic activity changes with time.

The radial waveform for azimuth θ, $u_h(\theta,t)$, is

$$u_h(\theta,t) = \cos\theta u_n(t) + \sin\theta u_e(t), \tag{1}$$

where t is the time, and $u_n(t)$ and $u_e(t)$ are the ground motions in the NS and EW components, respectively. The correlation coefficient between the 90°-phase-shifted vertical ground motion and radial ground motion in the azimuth θ, $D(\theta)$, is given by

$$D(\theta) = \frac{\int u_z^*(t)\, u_h(\theta,t)\, dt}{\sqrt{\int \left[u_z^*(t)\right]^2 dt}\sqrt{\int \left[u_h(\theta,t)\right]^2 dt}}, \tag{2}$$

where $u_z^*(t)$ is the 90°-phase-shifted vertical ground motion. The azimuth θ of the peak correlation coefficient is determined to be the apparent radial direction of the Rayleigh waves at the station. The expanded description on the analysis is presented in the supplementary materials.

2.2. Array beamforming analysis

We detect coherent seismic energy over stations using an array analysis to determine the incoming direction and phase velocity [37,38]. The crosscorrelation function of the ground motions between stations provides information on the interstation phase delay time that may depend on the incident direction and phase velocity. The crosscorrelation function of the ground motions is given by [39]

$$C_{ij}(\tau) = \frac{\int u_{z,i}(t) u_{z,j}(t+\tau) dt}{\sqrt{\int \left[u_{z,i}(t)\right]^2 dt}\sqrt{\int \left[u_{z,j}(t+\tau)\right]^2 dt}}, \tag{3}$$

where $C_{ij}(\tau)$ is the crosscorrelation coefficient between stations i and j for delay time τ, t is the time, and $u_{z,i}(t)$ and $u_{z,j}(t)$ are the vertical ground motions at stations i and j, respectively.

We perform slant-stacking of the crosscorrelation functions among the station pairs:

$$B(\vec{s}) = \sum_{i,j} C_{ij}(\vec{s}\cdot\vec{l}_{ij}), \tag{4}$$

where $B(\vec{s})$ is the slant-stacked crosscorrelation coefficient for slowness $\vec{s}$ and $\vec{l}_{ij}$ is the relative location of station j with respect to station i. The slant-stacked crosscorrelation coefficient is the maximum at the slowness of the incoming phase. Further information on the analysis is presented in the supplementary materials.

2.3. Source strength inversion

The microseisms observed at a station may be composed of energy from multiple sources. The Rayleigh-wave energy in microseisms is inferred from the power spectral density:

$$M_i(\mathbf{c}) = \sum_j^n m_{ij}, \tag{5}$$

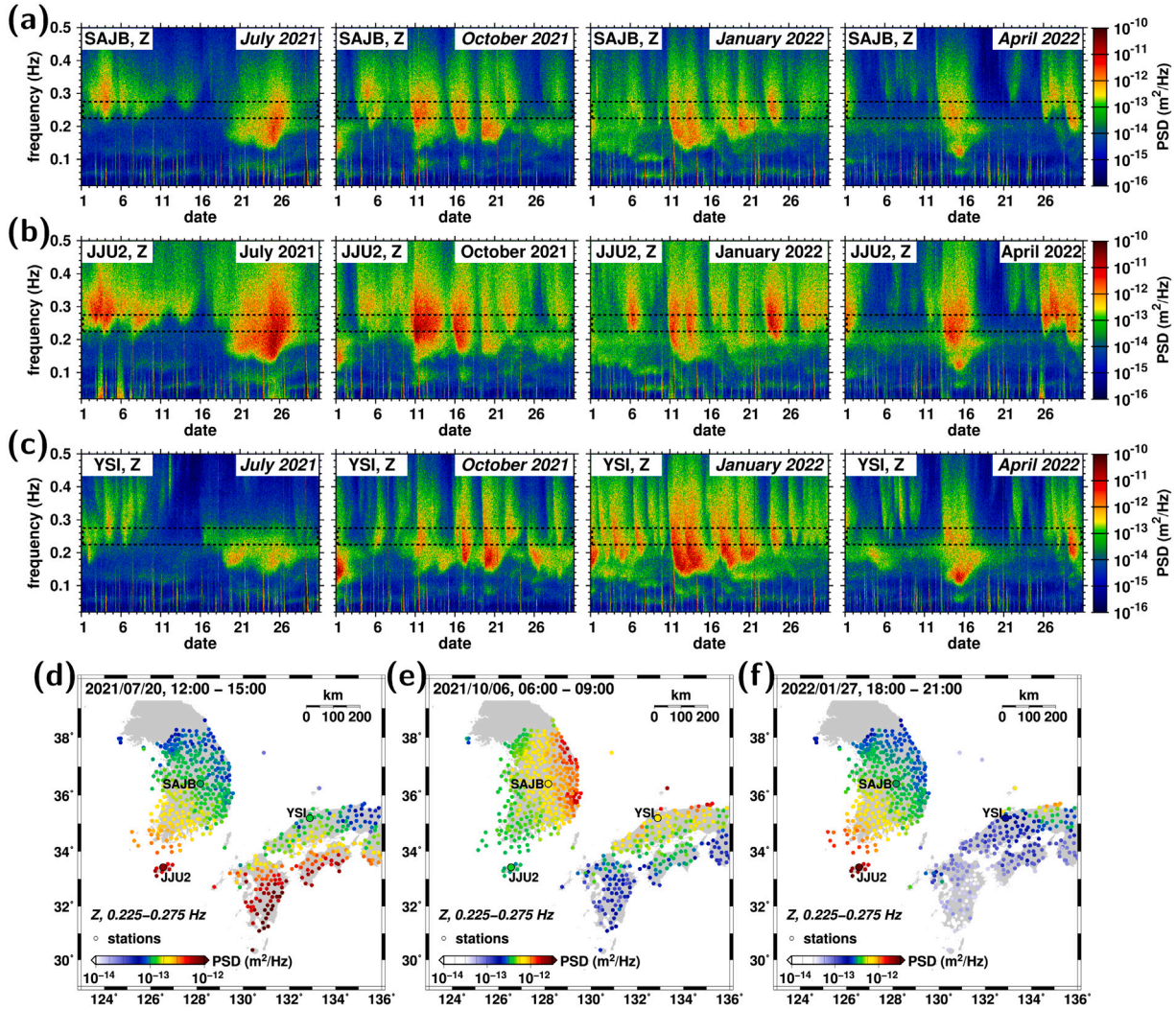

Fig. 3. Power spectral densities (PSDs) of vertical ground motions of ambient noises in July 2021, October 2021, January 2022, and April 2022 at stations (a) SAJB, (b) JJU2, and (c) YSI. Prominent secondary microseism energy is present at frequencies between 0.225 and 0.275 Hz (dotted boxes). The microseism amplitudes change with time. Spatial distributions of power spectral densities at frequencies of 0.225–0.275 Hz in (d) 12:00–15:00 on 20 July 2021, (e) 6:00–9:00 on 6 October 2021, and (f) 18:00–21:00 on 27 January 2022. Stations SAJB, JJU2, and YSI are marked on the maps. The microseism energy presents substantial spatiotemporal variation.

where $M_i(\mathbf{c})$ is the power spectral density of microseisms (m^2/Hz) at station i for a set of source strengths $\mathbf{c}$, n is the number of sources, and m_{ij} is the energy contribution of source j to station i.

The energy contribution m_{ij} is given by [40,41]

$$m_{ij} = c_j R_{ij}^{-1} \exp\left(-\gamma_{ij} R_{ij}\right), \tag{6}$$

where c_j is the strength of source j (m^3/Hz) to yield the energy contribution through the attenuation, R_{ij} is the horizontal distance (km) between station i and source j, and γ_{ij} is the representative attenuation factor (km^{-1}) on the path between the source and station.

The representative attenuation factor accounts for the anelastic energy loss and scattering in medium. The representative attenuation factor γ_{ij} is given by

$$\gamma_{ij} = \frac{1}{R_{ij}} \int_{Rij} \gamma(r) dr \tag{7}$$

$$= \frac{1}{R_{ij}} \int_{R_{ij}} \frac{2\pi f}{v(r) Q(r)} dr, \tag{8}$$

where r is the distance (km) along the path between station i and source j, f is the frequency (Hz), $\gamma(r)$ is the attenuation factor (km^{-1}) at location r, $v(r)$ is the group velocity (km/s) at location r, and $Q(r)$ is the quality factor at location r [40,41].

We determine the strengths $\mathbf{c}$ of distributed sources in uniformly discretized medium to minimize the objective function $S(\mathbf{c})$:

$$S(\mathbf{c}) = \sum_{i}^{N} \left[\ln\left(O_i\right) - \ln\left(M_i(\mathbf{c})\right)\right]^2 + \left[\omega_1 \nabla \mathbf{c}\right]^2 + \left[\omega_2 \nabla^2 \mathbf{c}\right]^2, \tag{9}$$

where N is the number of stations, O_i is the observed energy (m^2/Hz) of the vertical ground motions at station i, and ω_1 and ω_2 are constants to control the first and second derivative smoothing. The smoothing parameters ω_1 and ω_2 are determined to be 5 and 50 from synthetic tests (supplementary materials).

3. Microseism properties

Microseisms may be influenced by composite effects of regional environments and oceanic conditions. The Korean Peninsula and Japanese islands are surrounded by the Yellow Sea, South Sea, East Sea (Sea of Japan), Philippine Sea, and Pacific Ocean (Figs. 1 and S1 in supplementary materials). The ocean depths are shallow in the Yellow Sea and South Sea (≤ 200 m), while they are large in the Pacific Ocean and Philippine Sea (up to ~10 km). The ocean depths in the East Sea are ~2 km in the Ulleung Basin and Yamato Basin, and ≤ ~1 km in the Korea Plateau, Oki Bank, and Yamato Rise (Figs. 1 and S1 in supplementary materials).

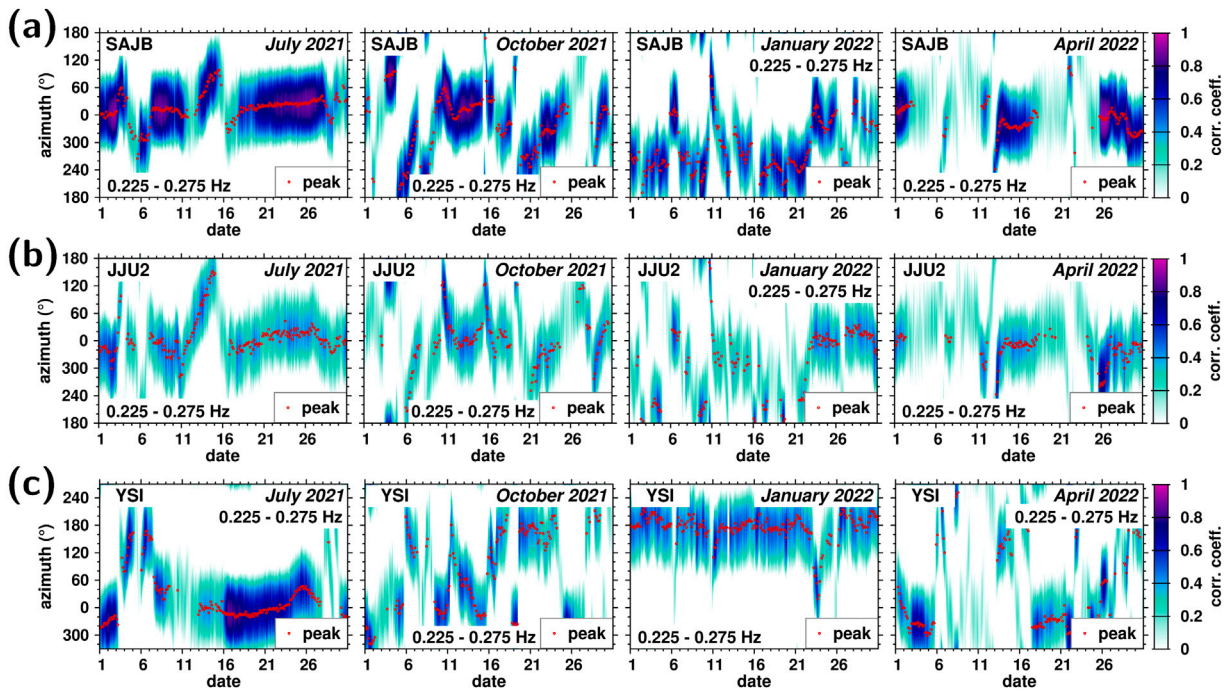

Fig. 4. Rayleigh-wave polarization analysis for microseisms at frequencies of 0.225–0.275 Hz in July 2021, October 2021, January 2022, and April 2022 at stations (a) SAJB, (b) JJU2, and (c) YSI. The correlation coefficients between the horizontal ground motions and 90°-phase-shifted vertical ground motions are presented as a function of azimuth and time. The azimuth with peak correlation coefficient indicates the apparent radial direction of the Rayleigh waves in microseisms (dots). The radial directions differ by station, changing with time.

These regions are affected by the east Asian monsoon system, which drives seasonal variation in atmospheric pressure, wind field, and ocean wave distribution (Figs. 2 and S2 in the supplementary materials). Strong southeasterly winds over the South Sea, East China Sea, and northwestern Pacific develop ocean waves in the summer. The northeasterly winds in the northwestern Pacific near the southern and eastern Japanese islands increase ocean waves in the fall. In the winter, northwesterly winds generate intense ocean waves in the East Sea and northwestern Pacific. Also, mild wind fields and ocean waves develop in the region off the eastern Japanese islands in the spring. These seasonal winds and ocean waves occur periodically (Fig. S2 in the supplementary materials).

We investigate the microseism properties and temporal evolution and seasonality from summer 2021 to spring 2022. We select a month from each season including July 2021 for summer, October 2021 for fall, January 2022 for winter, and April 2022 for spring. The selected periods are not affected by major extreme weather events such as typhoons and extratropical cyclones, featuring representative seasonal characteristics (supplementary materials). The microseisms are affected by dispersive ocean waves, presenting frequency-dependent property variations [34,42] (Fig. 3). We primarily focus on the microseisms in the most dominant frequencies (0.225–0.275 Hz) (Fig. 3).

We analyze continuous three-component seismic records from 476 seismic stations around the Korean Peninsula and southwestern Japanese islands (Fig. S1 in supplementary materials). The continuous records are divided into three-hour-long segments that are bandpass-filtered in 0.225–0.275 Hz after instrument-response correction. We assess the microseism amplitudes at the stations using the power spectral densities of the vertical ground motions. The energy influx orientations in the microseism field are determined from the elliptical polarization of the Rayleigh waves (Fig. 4). We use 40-s waveform windows for the Rayleigh-wave polarization analysis. We stack the estimates for representative results. We construct microseism-energy flow paths from discrete microseism influx directions (Fig. 5). We present additional information on the analysis in the supplementary materials.

The microseism amplitudes observed at individual stations change with time. The microseism properties exhibit frequency-dependent features [19,21], changing with temporal ocean-wave evolution [21,32] (Figs. 1 and 2). The temporal variation in microseism amplitudes suggests that the microseism sources evolve with time. However, the waveform records suggest that the microseisms are persistently present despite the temporal changes (Fig. 3).

We estimate the amplitudes and orientations of the microseism influxes at stations from the Rayleigh waves in microseisms (Figs. 1, 3, and 5). The amplitudes and influx orientations change gradually with time. The feature suggests temporal changes in microseism source compositions, implying independent multiple microseism sources with temporally-changing effective strengths (Fig. 5). There may be multiple dominant microseism sources. The compositions of contributing sources change by observation site depending on the relative distance and strength of source, constructing gradually-varying energy flows. When the energy from multiple sources with comparable strengths is mixed, the polarization of microseisms appears to be weak at the observation site.

The polarization of microseisms presents a transient microseism influx. We determine the apparent energy flow of microseisms (Fig. 5). The microseism energy is radiated radially from the source locations. Thus, the microseism source locations can be determined from the orientation of energy flux. The energy flows are discontinuous between the Korean Peninsula and the southwestern Japanese islands, suggesting the differences in influencing sources. The observed microseism energy is relatively weak in inland regions compared to coastal regions. The energy flow orientation and location-dependent energy strengths suggest the presence of effective coastal microseism sources (Fig. 5). Coastal microseism sources may be more effective in the composition of observed microseism energy than pelagic microseism sources.

Notably, while there are temporal variations, the dominant energy-flux orientation is north to west. The observation suggests that the principal microseism sources are located near the east and south coasts of the Korean Peninsula (Fig. 5). In the southwestern Japanese islands,

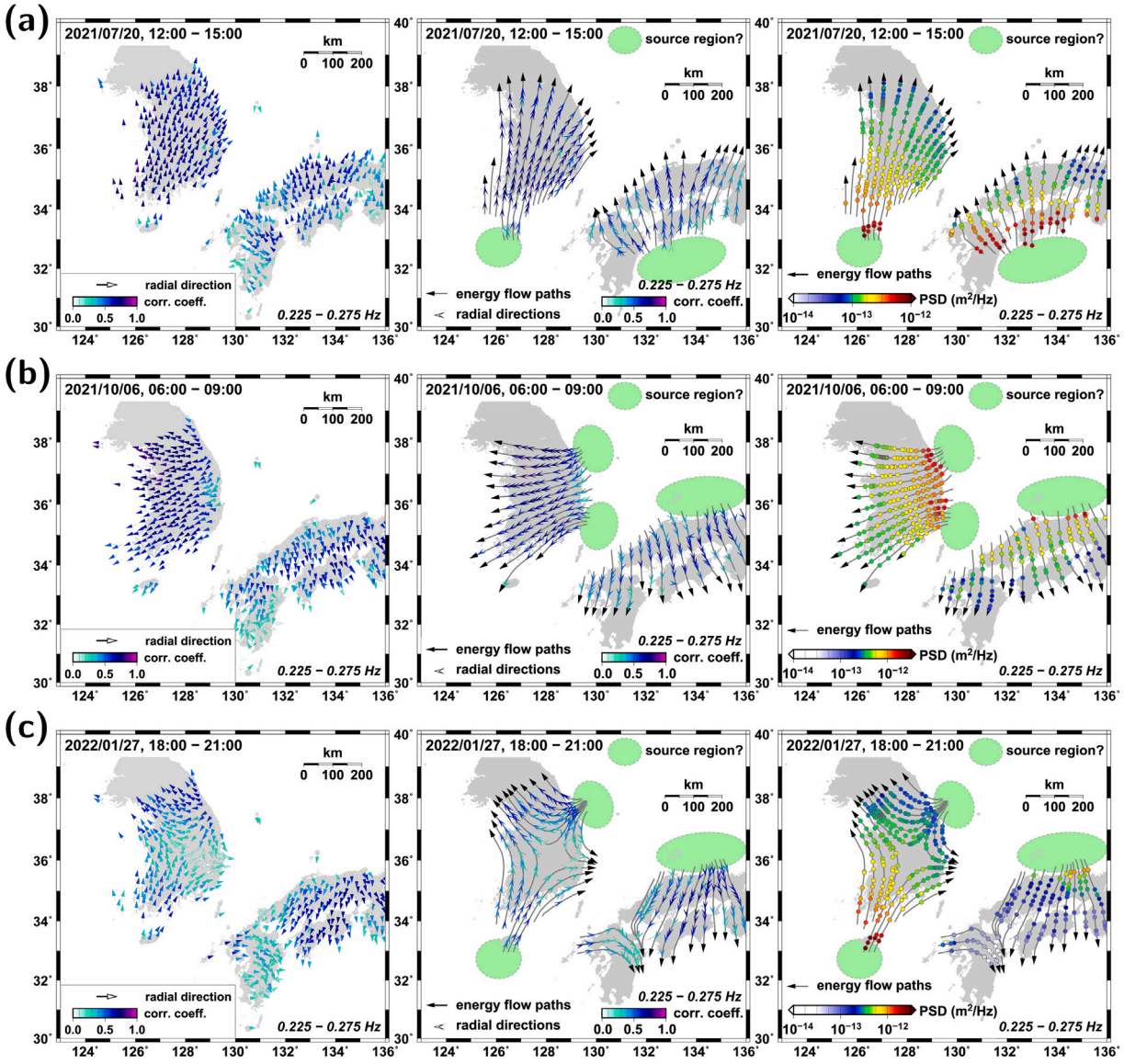

Fig. 5. Transient microseism energy flow in (a) 12:00–15:00 on 20 July 2021, (b) 6:00–9:00 on 6 October 2021, and (c) 18:00–21:00 on 27 January 2022. (left) Spatial distributions of radial directions of Rayleigh waves in microseisms at stations, (middle) apparent energy flow paths (solid lines) of Rayleigh waves in microseisms, and (right) microseism amplitude distributions along the energy flow paths are presented. The Rayleigh-wave radial directions (arrows) and vertical power spectral densities (PSDs; circles) are displayed. Apparent microseism source regions are marked (shaded regions; R1, R2, R3, R4, and R5).

energy flux is predominantly oriented in north-south, suggesting the presence of major sources around the southern and northern coasts (Fig. 5). These observations suggest that the effective microseism sources are localized, developing characteristic regional microseism energy flux.

4. Microseism source distribution

We determine the strengths of individual microseism sources from the microseism energy observed at the stations (Fig. 6 and supplementary movies 1–4). The microseism source-strength inversion determines the locations and strengths of individual microseism sources (Figs. S3-S6 in supplementary materials). The microseism source locations are searched over discretized cells in oceanic regions (Fig. S3). We iteratively search a set of source locations and source strengths to yield the observed microseism field in inland regions (Figs. S5 and S6 in supplementary materials). We iteratively update the source model to minimize the residuals between the observed and theoretical microseism energy at the stations (Figs. S5 and S6 in supplementary materials). Synthetic recovery tests are performed to examine the validity of the inverted source model (Figs. S7 and S8 in supplementary materials).

The inverted source field suggests concurrent excitation of multiple individual sources with temporally-varying strengths (Figs. 6 and 7). The inverted microseism source locations agree with the microseism energy flow paths. The observation is also supported by the results of array beamforming analysis (Figs. 6 and 7). The microseism sources gradually evolve with time (Figs. 8 and S9). The microseism source distribution is correlated with the ocean wave amplitudes, suggesting a role of ocean waves in developing microseism sources (Figs. 6, 7, 8, and S9).

The microseism sources are relatively weak when ocean waves are small (Fig. S9(a)). The microseism sources are strong when the ocean waves are large around the coast (Fig. S9(b)). The microseism source strength grows with the ocean wave amplitude (Fig. S9(c)–(h)). The observation suggests that the evolution of ocean waves causes the temporal variation in microseism source distribution. The microseism

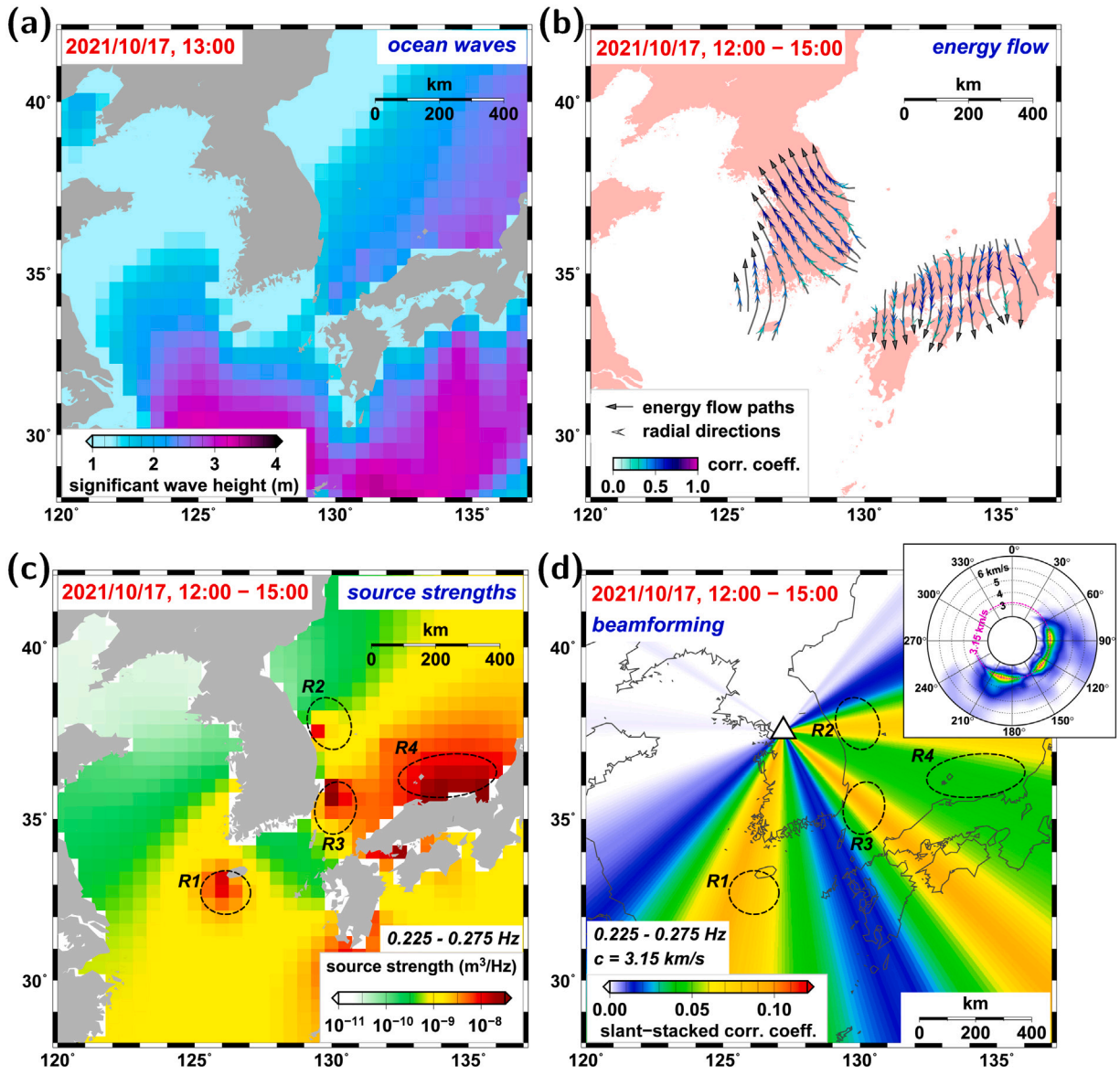

Fig. 6. (a) Ocean wave heights and (b) apparent microseism energy flow paths (solid lines) in 12:00–15:00, October 17, 2021. The microseism energy flow paths inferred from Rayleigh-wave polarization directions are presented (arrows). (c) Microseism source distribution in 12:00–15:00, October 17, 2021. Prominent microseism sources are indicated (regions R1–R5). The ocean wave heights and microseism source strengths are spatially correlated. (d) Example of array beamforming analysis for microseism energy at a single station. The slant-stacked interstation waveform correlation coefficients as a function of backazimuth and phase velocity (c) are presented (inset). The array beamforming analysis suggests that the observed local microseism energy is dominantly influenced by near-distance microseism sources.

sources may develop in different manners that vary by region [16, 32], depending on the regional medium properties [41,43]. Coastal microseism sources are stronger than pelagic microseism sources with comparable ocean wave heights (Figs. 7, 8, and S9). Coastal offshore regions naturally have shallow ocean depths and uphill slopes that may promote the microseism development [11,14].

The microseism sources are prominent in regions of high ocean waves such as the East Sea, South Sea, and Philippine Sea, while weak in regions with small ocean waves, such as the Yellow Sea (Figs. 7, 8, and 9(a)). The estimated microseism source locations are correlated with the oceanic environment. The microseisms develop strongly in shallow oceanic regions such as the Korea Plateau and Oki Bank, while are weak in deep oceanic regions such as the Ulleung Basin and Yamato Basin (Fig. 9(b)). Lateral variations in medium properties may further affect the generation of microseisms [12,16]. The combined effects of the ocean waves and regional properties construct localized microseism sources.

We observe prominent microseism sources around Jeju Island (region R1), the east and southeast coasts of the Korean Peninsula (regions R2 and R3), and the south and north coasts of the southwestern Japanese islands (regions R4 and R5) (Figs. 7 and 8). The microseism sources appear to be stationary in space. The source strengths change with time. The stationary sources with temporally-varying strengths build complex microseism fields with temporally-varying polarization directions and amplitudes [13,32]. The observed feature, being contrast with the traditional view, suggests that the microseism sources migrate with time.

We examine seasonal characteristics of microseism sources by stacking the microseism source distribution by season. The stacked distribution presents the seasonal representative microseism source distribution (Figs. 10, S10, and S11 in supplementary materials). The microseism

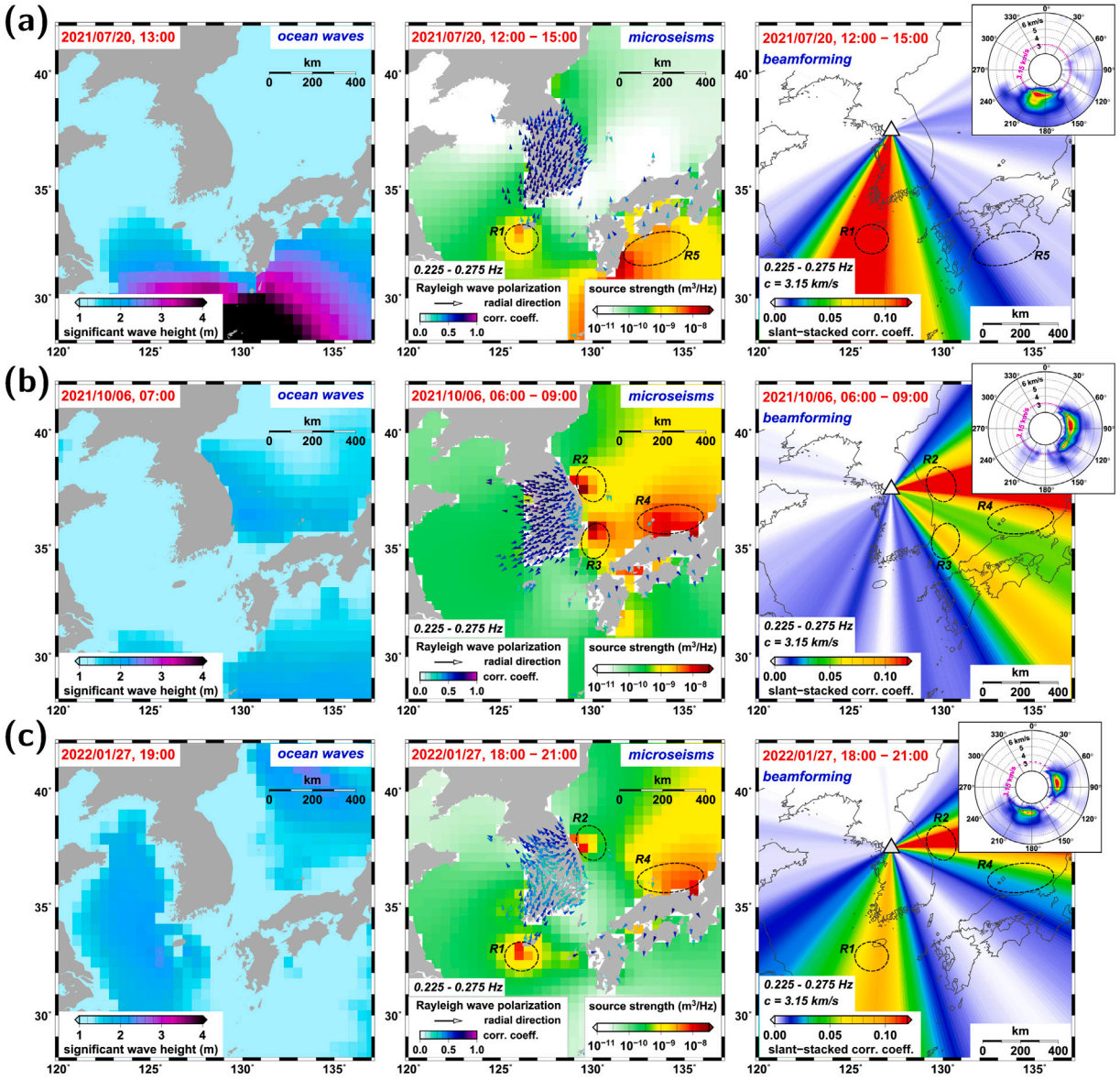

Fig. 7. Microseism source distribution. Comparison among ocean wave heights, microseism source strengths, and microseism energy influx orientations for time periods of (a) 12:00–15:00 on July 20, 2021, (b) 6:00–9:00 on October 6, 2021, and (c) 18:00–21:00 on January 27, 2022 is presented. (left) Ocean wave heights, (middle) microseism source strengths and radial directions of Rayleigh waves in microseisms (arrows), and (right) examples of array beamforming analysis of microseism energy at a single station is displayed. The slant-stacked interstation waveform correlation coefficients are presented as a function of backazimuth and phase velocity (c) (inset). Prominent source locations are marked (R1–R5).

sources present apparent seasonal variations, which may be attributed to the seasonality of ocean waves (Fig. 2). The representative microseism source distribution presents localized prominent microseism sources (regions R1–R5). Notably, the prominent sources appear to be nearly stationary across seasons. However, the strengths of stationary sources vary by season (Table S1 in supplementary materials) (Figs. 10 and S12 in supplementary materials).

In the summer of 2021, the microseism sources have peak source strengths of 7.5×10^{-9} m^3/Hz around Jeju Island (region R1) and 5.4×10^{-9} m^3/Hz around the southwestern Japanese islands (region R5) (Fig. 10(a)). In the fall of 2021, the prominent microseism sources have peak source strengths of 1.2×10^{-8} m^3/Hz in region R1, 4.9×10^{-9} m^3/Hz in region R2, 4.2×10^{-9} m^3/Hz in region R3, and 2.6×10^{-8} m^3/Hz in region R4 (Fig. 10(b)).

In the winter of 2022, the microseism sources have peak source strengths of 4.8×10^{-9} m^3/Hz in region R1, 5.7×10^{-9} m^3/Hz in region R2, 2.1×10^{-9} m^3/Hz in region R3, and 8.5×10^{-8} m^3/Hz in region R4 (Fig. 10(c)). In the spring of 2022, the microseism sources have peak source strengths of 1.9×10^{-9} m^3/Hz in region R1, 5.1×10^{-9} m^3/Hz in region R3, and 1.5×10^{-8} m^3/Hz in region R4 (Fig. 10(d)).

Notably, we find that the seasonal microseism source distribution is correlated with seasonal variation in ocean wave activity (Figs. 2, 10, and S10 in supplementary materials). In the summer, the microseism sources become pronounced near the South Sea, East China Sea, and the northwestern Pacific (e.g., regions R1 and R5), which is consistent with strong ocean waves in those regions. We observe strong microseism sources in the East Sea (e.g., regions R2, R3, and R4) in the winter. In the fall, the microseism sources around the South China Sea, South Sea, and East Sea (regions R1–R4) present comparable strengths. The ocean waves are relatively weak in the spring, developing mild microseism sources. The microseism source strengths present a seasonal variation.

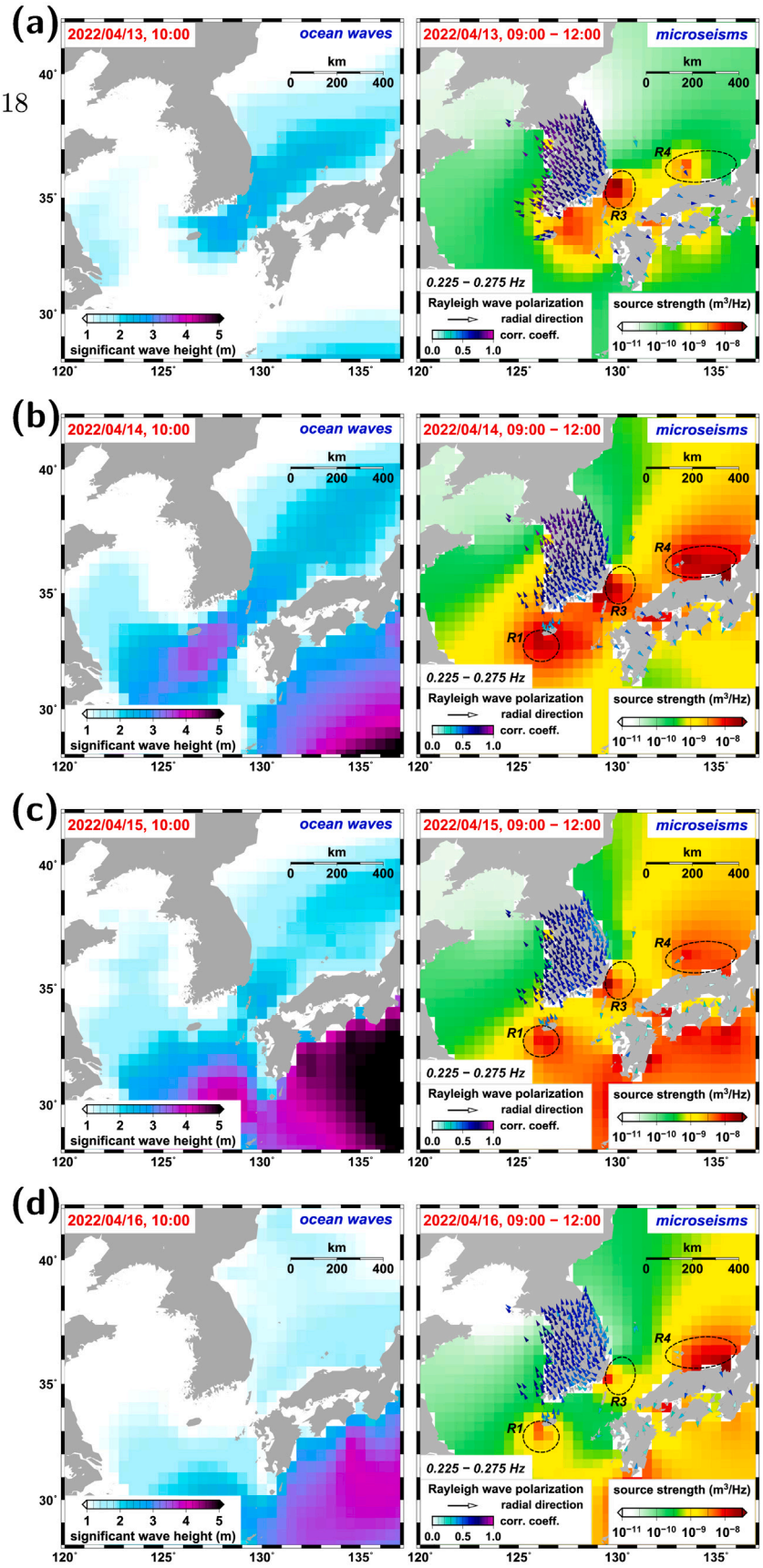

Fig. 8. Temporal evolution of microseism sources. Comparison between ocean wave heights and microseism source strengths for consecutive time periods of (a) 9:00–12:00 on April 13, 2022, (b) 9:00–12:00 on April 14, 2022, (c) 9:00–12:00 on April 15, 2022, and (d) 9:00–12:00 on April 16, 2022. (left) Ocean wave heights and (right) microseism source strengths are presented. The radial directions of Rayleigh waves in microseisms at stations are indicated (arrows). Prominent source regions are marked (R1–R5). The microseism sources evolve with time, depending on the ocean waves.

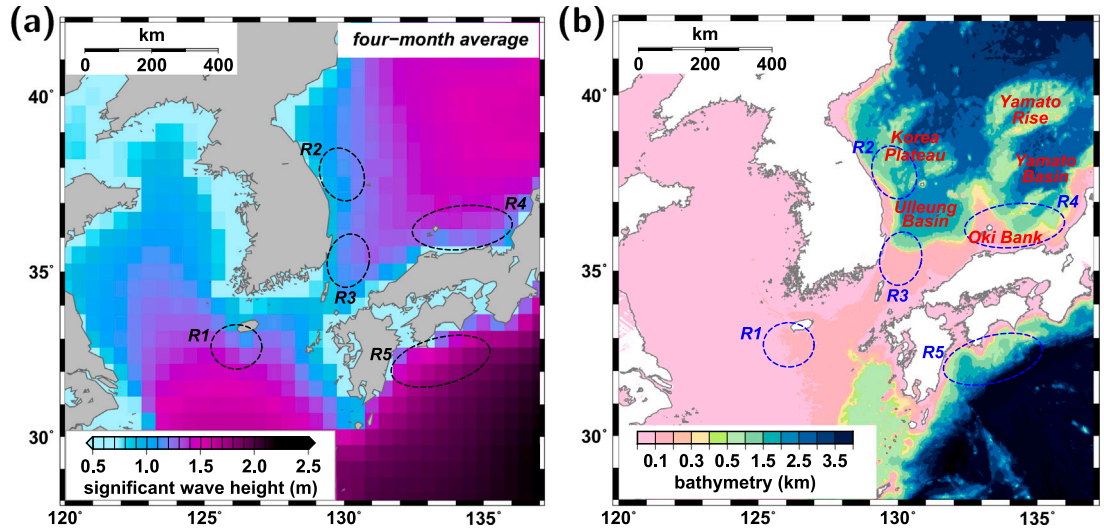

Fig. 9. (a) Comparison between microseism source locations and ocean wave heights. Prominent microseism source regions (R1–R5) are marked over the average ocean-wave heights in four months of July 2021, October 2021, January 2022, and April 2022. The microseism sources develop effectively near the coasts with high ocean waves. (b) Comparison between microseism source locations and oceanic environment. Major oceanic structures are indicated. The microseism sources develop prominently in shallow oceanic regions, while are weak in deep oceanic regions.

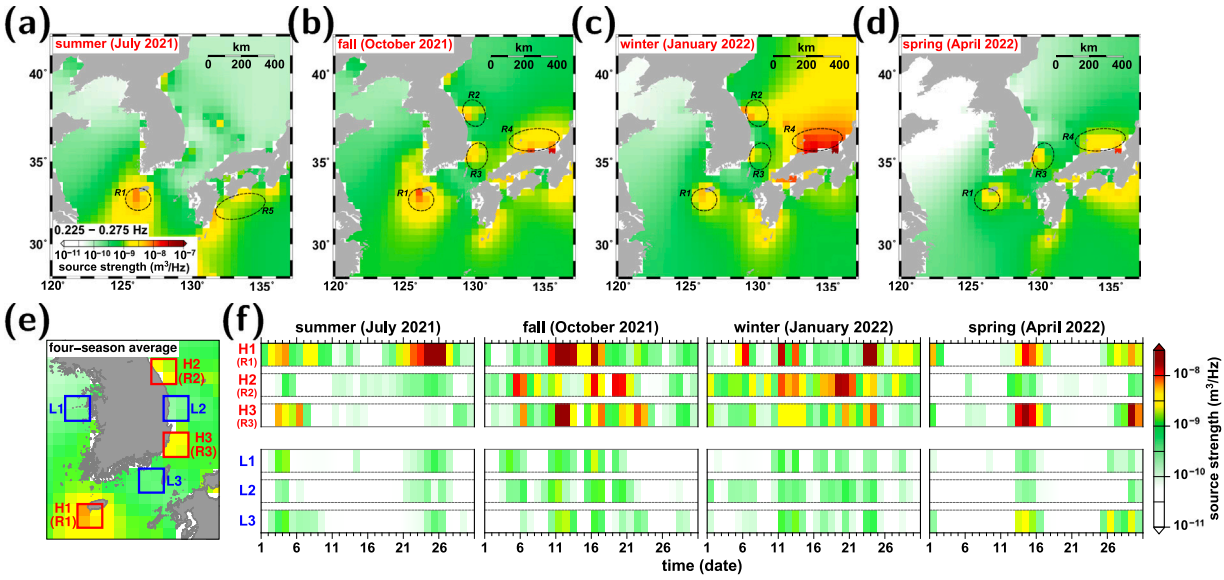

Fig. 10. Seasonal variations in microseism sources in (a) the summer of 2021 (July 2021), (b) fall of 2021 (October 2021), (c) winter of 2022 (January 2022), and (d) spring of 2022 (April 2022). The microseism sources significantly vary by season. The prominent microseism sources are stationary across seasons with varying strengths (regions R1–R5). (e) Enlarged four-season average source-strength map. Prominent microseism source regions (H1 (R1), H2 (R2), and H3 (R3)) are marked. Insignificant microseism-inducing regions (L1, L2, and L3) are marked for comparison. (f) Temporal variations in microseism source strengths are presented. The prominent source regions (H1 (R1), H2 (R2), and H3 (R3)) excite strong and consistent energy in all seasons.

We, however, observe prominent microseism sources (H1, H2, and H3) that are effective continuously over the year (Fig. 10(f)). On the other hand, microseism energy is rarely excited at some regions (L1, L2, and L3) (Fig. 10(f)).

Occasional extreme weather events such as extratropical cyclones and typhoons may develop anomalous microseisms that are different from the microseisms in usual oceanic conditions [21,22]. We examine the microseism feature during the passage of typhoon. We consider typhoon Hinnamnor in 2022, a Category 5 typhoon according to the Joint Typhoon Warning Center (JTWC) (Fig. 11). The central pressure was 930–980 hPa. The typhoon passed over the oceanic regions around the Korean Peninsula in September 5 to 6, 2022. We observe strong stationary microseism sources along the typhoon track during the passage (Fig. 11). The strengths of effective microseism sources change with the typhoon passage (e.g., regions R1, R2, and R3) (Fig. 11). This observation suggests that environmental factors control the development of microseism sources.

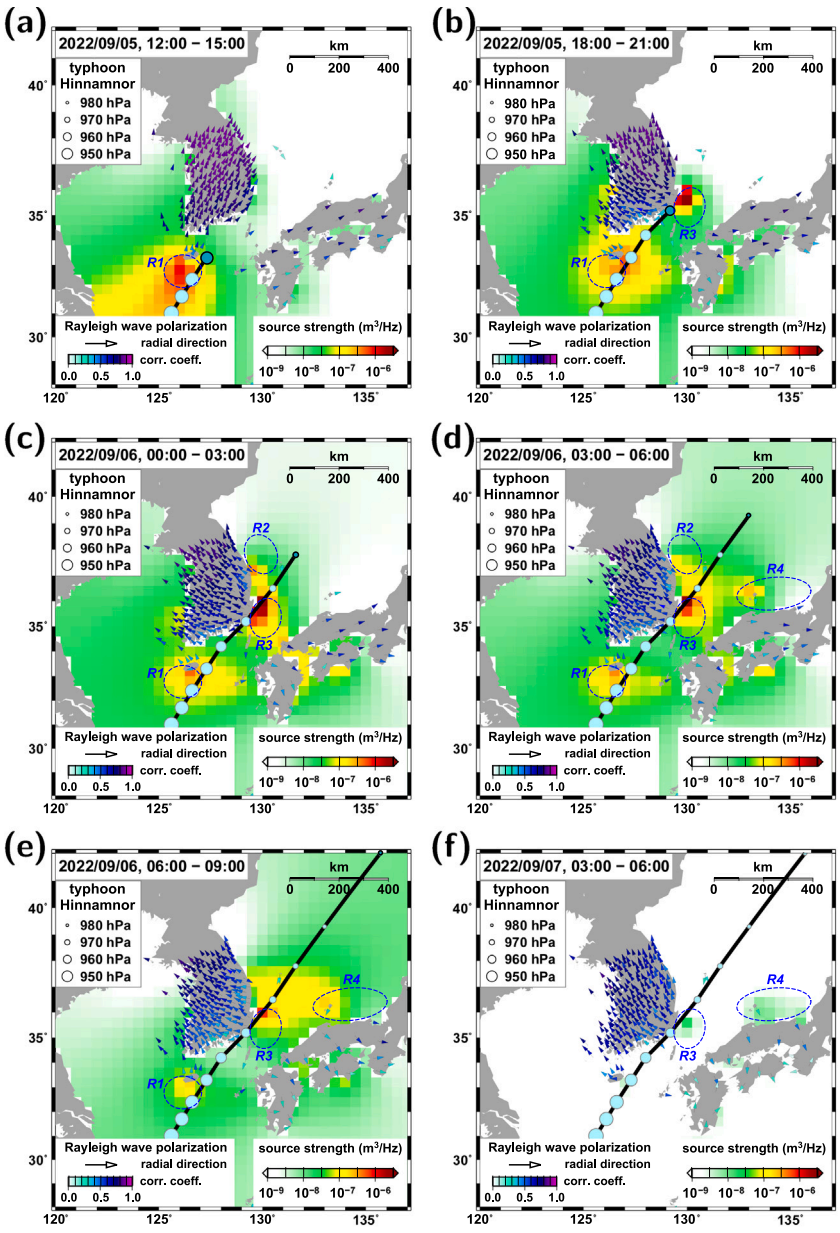

Fig. 11. Temporal evolution of microseism sources during the passage of typhoon Hinnamnor in 2022. Microseism source strengths and radial directions of Rayleigh waves in microseisms (arrows) are presented for periods of (a) 12:00–15:00 on September 5, 2022, (b) 18:00–21:00 on September 5, 2022, (c) 0:00–03:00 on September 6, 2022, (d) 3:00–06:00 on September 6, 2022, (e) 06:00–09:00 on September 6, 2022, and (f) 03:00–06:00 on September 7, 2022. The trajectory (thick solid line) and location of typhoon Hinnamnor (closed circle) are marked. The prominent source regions are indicated (R1–R4). Strong microseism sources develop during the typhoon passage.

5. Unrelenting microseism influx

The stationary microseism sources explain the nature of microseism fields. Multiple microseism sources at different locations in various azimuths collectively contribute to the inland microseism field. The contribution effects of individual microseism sources are dependent on the source strengths and distances to the observation sites. The influences of individual microseism sources decrease with increasing distance due to microseism energy attenuation (Fig. S4; see supplementary materials). The microseism energy decay exponentially with distance due to the geometrical spreading, scattering, and anelastic energy loss (Fig. S4 in supplementary materials). Thus, the microseism field at a site is dominantly influenced by near-distance sources.

The prominent microseism sources (regions R1–R5) are spatially invariant with time, producing microseism fields with strong directivity in certain backazimuths (Fig. 12). The energy flux orientations are primarily controlled by the dominant microseism sources (Fig. 12). The relative compositions of the contributing sources change seasonally (Figs. 12 and 13). The orientation of microseism influx energy corresponds to the direction toward the dominant sources of the time, being sustained over the season (Table S2 in supplementary materials).

The microseism field in the Korean Peninsula is dominantly influenced by the sources around Jeju Island (region R1) and the east and southeast coasts of the Korean Peninsula (regions R2 and R3) (Figs. 10 and 13). In the central Korean Peninsula (site K1), the microseism field is dominated by the influx energy at backazimuths around 30°, 120°, and 210°. In the summer, the influx energy is mainly oriented in backazimuths around 210°. During the fall, the energy predominantly flows in backazimuths around 210°, and partly in backazimuths around 30° and 120°. Also, we observe comparable energy fluxes at backazimuths

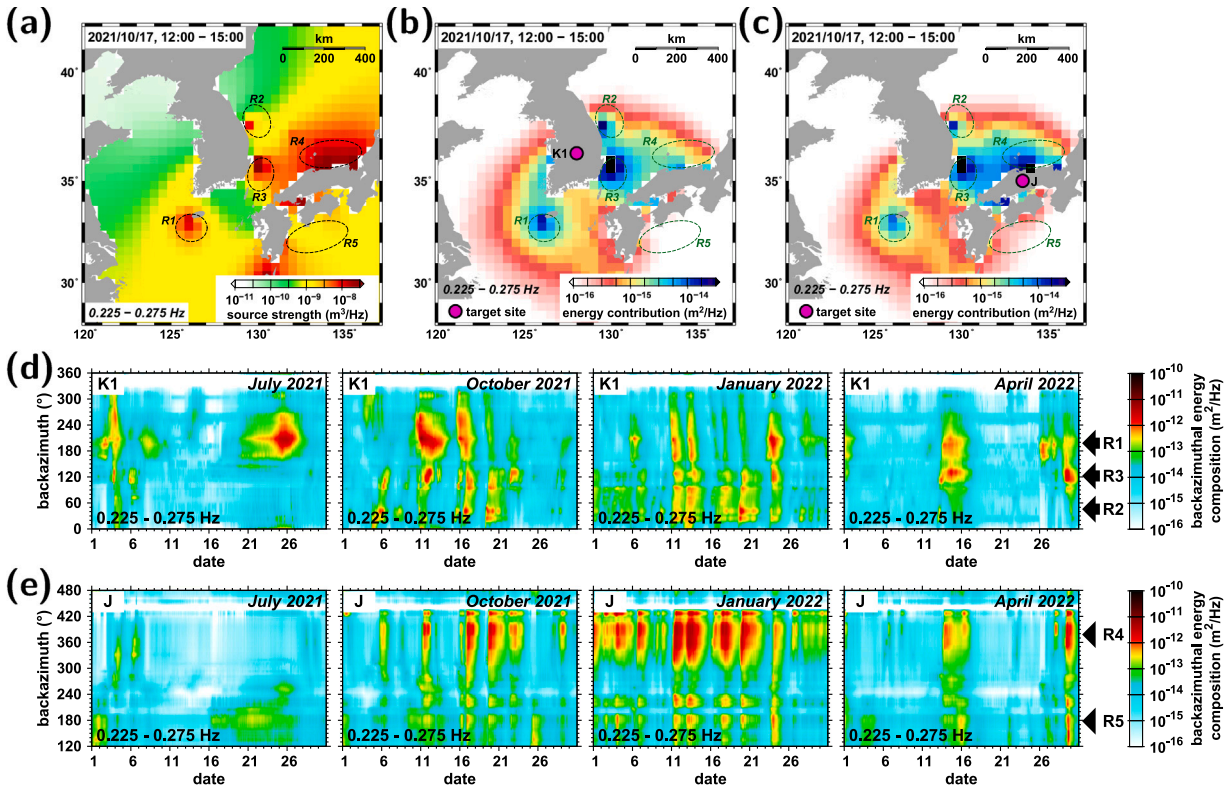

Fig. 12. Energy contributions of individual microseism sources: (a) Microseism source strengths, and individual source contributions at sites (b) K1 and (c) J in 12:00–15:00, October 17, 2021. Prominent microseism source locations are marked (R1–R5). Temporal variations in energy influx orientations at sites (d) K1 and (e) J. The energy influx orientations for the prominent microseism sources are indicated (arrows).

around 30°, 120°, and 210° in the winter and 120° and 210° in the spring (Fig. 13).

In the western Korean Peninsula (site K2), the dominant influx energy is primarily oriented in backazimuths of ~ 80° and ~ 190°, and partly in backazimuths of ~ 130°. During the summer, the influx energy dominantly originates from directions in backazimuths around 190°. In the fall, the influx energy is mainly oriented in backazimuths around 190° and partially in backazimuths around 80° and 130°. Similarly, in the winter, the microseism energy predominantly originates from backazimuths around 80° and fractionally from backazimuths around 130° and 190°. In the spring, comparable influx energy is observed in backazimuths around 130° and 190° (Fig. 13).

At site K3 in the eastern Korean Peninsula, the dominant influx energy is oriented in backazimuths of around 30°–100° and 200°, and fractional energy at backazimuths of around 150° (Fig. 13). In the summer, the dominant influx energy is oriented in backazimuths around 200°. During the fall, the microseism energy dominantly originates from directions in backazimuths around 30°–100° and 200°, with a partial contribution from directions in backazimuths around 150°. Similarly, in the winter, the influx energy is oriented in backazimuths around 30°–100° with fractional contributions in directions of backazimuths around 150° and 200°. During the spring, comparable influx energy is observed in backazimuths around 150° and 200° (Fig. 13).

At site K4 in the southwestern Korean Peninsula, we observe dominant influx energy at backazimuths of around 200°, and fractional energy at backazimuths of around 30° and 80°. Notable influx energy is observed in all seasons at backazimuths of around 200°. Also, at site K5 in the southeastern Korean Peninsula, we observe prominent influx energy at backazimuths of around 70°–130° and 220°, and fractional energy at backazimuths of around 10°. In the summer, the dominant influx energy is oriented in backazimuths of 220°. During the fall, winter, and spring, the microseism energy mainly originates from directions in backazimuths of around 70°–130° and 220°, and partly from directions in backazimuths of around 10°.

At site J in the southwestern Japanese islands, the microseism field is predominantly composed of influx energy from the northern offshore regions of the southwestern Japanese islands (region R4) in backazimuths of −30° to 40° and the southern offshore region of the southwestern Japanese islands (region R5) in backazimuths of 120° to 200°. The influx energy is strong in backazimuths of −30° to 40° in the fall, winter, and spring, and in backazimuths of 120° to 200° in the summer.

6. Discussion

The precise determination of microseism sources challenges the traditional view of microseism sources. The microseism sources are controlled by the combined effects of regional properties, resulting in development of stationary individual sources with temporally-varying strengths. Each individual stationary microseism source delivers azimuthally-polarized energy of temporally-varying strength. The microseism amplitude changes with time. However, the microseism energy flux field is persistent. The microseism field develops from stationary microseism sources.

The microseisms in the Korean Peninsula present average energy of ~4 × 10^{-13} m^2/Hz in the frequency band of 0.225–0.275 Hz per second, producing energy flux of ~2–15 × 10^{-7} W m^{-2} that varies by region (Fig. 14). Fractional stress changes of 1–10 kPa may trigger earthquakes in optimal conditions [44,45]. The microseisms induce dynamic stress changes over the region, which may trigger earthquakes in local regions. We find mild spatial correlations between microseism sources and earthquakes, suggesting possible seismicity induction by microseisms (Fig. S13; see supplementary materials).

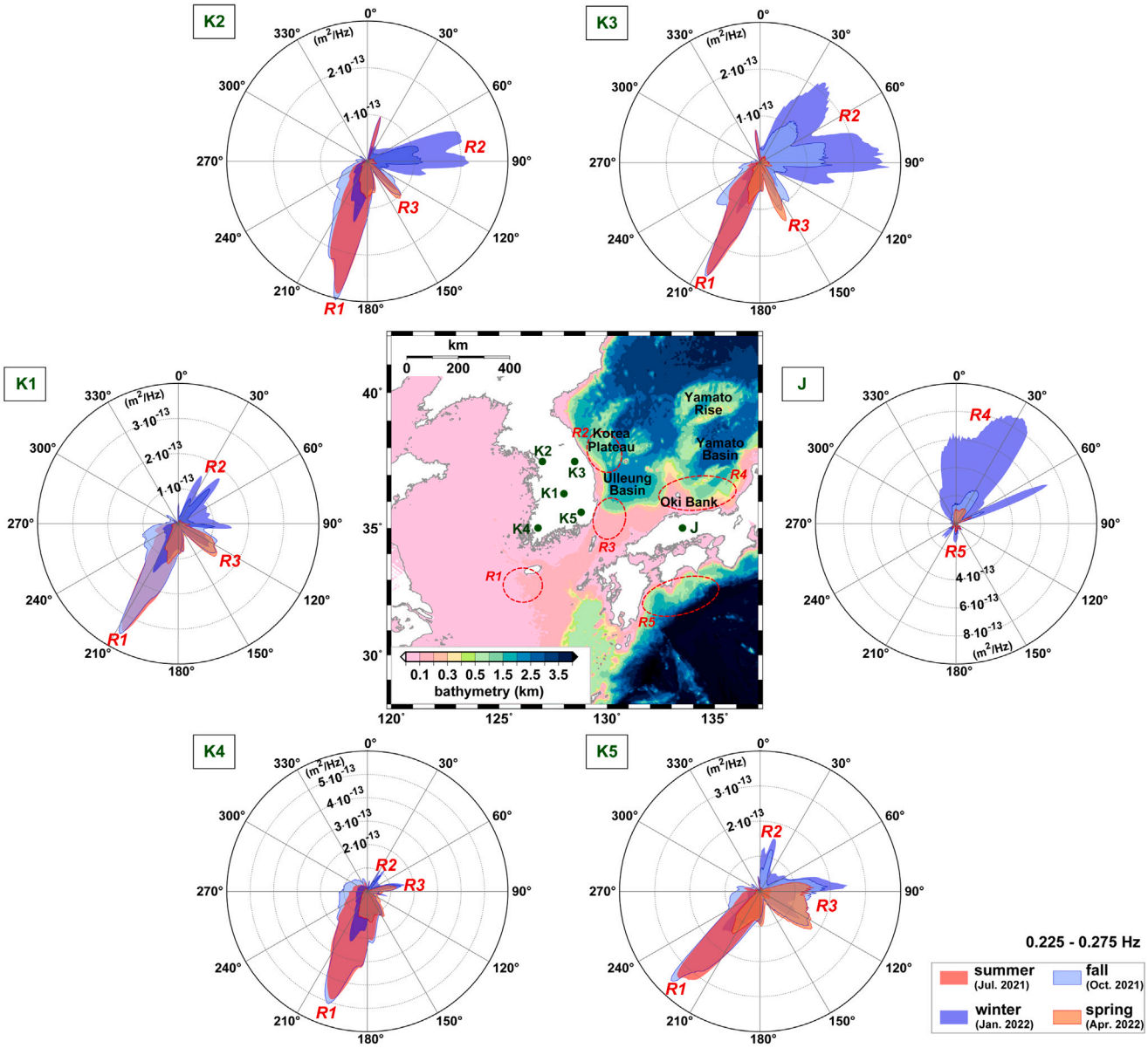

Fig. 13. Orientation of influx microseism energy. Backazimuthal compositions of microseism energy at six selected sites (K1, K2, K3, K4, K5, and J) for four seasons are presented. The site locations (closed circles) and prominent microseism source locations (regions R1–R5) are presented on the map. The seasonal orientations of the microseism energy are constant at individual sites.

The ubiquitous, unrelenting, and coherent nature of microseisms suggests their potentials as a natural energy resource. The peak influx energy in the microseism field may reach ~0.2–1.5 J/s over an area of 1 km^2 (equivalent to ~15–130 kJ per day, and ~5–47 MJ per year) (Fig. 14). The microseism energy is weak but consistent over a local region, yielding a considerable amount of energy. The microseism energy may be collected by piezoelectricity and electromagnetic induction devices, offering a renewable energy resource [7,8]. An aperture-array system composed of such devices may be used to collect energy. The energy conversion efficiency may depend on the alignment between the incoming microseism energy and energy-collection system. Given the consistent energy influx orientation, aligning the system may enhance the efficiency.

It is noteworthy that the accumulated energy is comparable to the energy consumption of a seismic sensor that is typically given by <~0.5 J/s, which corresponds to the microseism energy over an area of ~0.3–3 km^2 [46,47]. While the power density of microseisms is lower than that of conventional renewable energy sources such as solar [48,49] or wind energy [50,51], the microseisms present a unique advantage in remote or extreme environments where conventional energy sources are limitedly available.

While we consider the microseisms in a narrow frequency band (0.225–0.275 Hz), the overall properties of microseisms are consistent in the typical secondary-microseism frequency band (0.15–0.5 Hz) (see, Fig. S14 in the supplementary materials). The consistent properties in a wide frequency range support the potential for practical use of microseism energy. Since the microseism development is influenced by local conditions, the optimal energy harvesting system may be site-dependent. Also, extreme weather events such as typhoons may temporarily induce intense microseism energy.

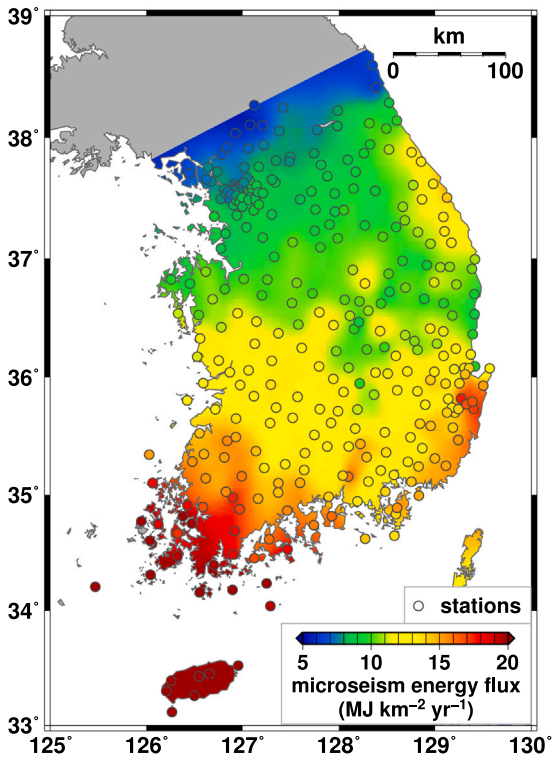

Fig. 14. Average microseism energy fluxes over four seasons (summer of 2021, fall of 2021, winter of 2022, and spring of 2022). The peak energy flux reaches ~5–47 MJ km^{-2} yr^{-1}.

7. Conclusions

Understanding the nature of microseisms is essential to examine the potentials as an energy resource. We examined the detailed properties of microseisms around the Korean Peninsula and the southwestern Japanese islands from summer 2021 to spring 2022. We characterized the energy flow directions, intensity, and attenuation of microseisms. We illuminated the microseism source locations using a source strength inversion method. The microseism source locations were confirmed by array beamforming analysis. The analyses presented the nature of microseisms.

We observe unrelenting microseisms in inland regions. The amplitudes and orientations of microseism energy flux gradually change with location. The microseism energy, gradually decreasing with distance, flows from the coasts to inland areas. These features suggest that dominant microseism sources are located near the coasts. The amplitudes and energy flow orientations change with time, suggesting temporal evolution of microseism sources.

We invert the microseism source distribution from the energy flows, demonstrating excitation and radiation patterns of microseisms. The microseism source locations are apparently correlated with ocean wave distribution. The microseism source distribution changes gradually with time in accordance with the temporal evolution of ocean waves, suggesting that ocean waves play a crucial role in the microseism excitation. The seasonal variation in ocean waves leads to temporal changes in microseism sources.

The microseisms develop strongly in particular coastal regions that include offshore regions around Jeju Island, the east and southeast coasts of the Korean Peninsula, and the north and south coasts of the southwestern Japanese islands. These localized dominant sources remain stationary over time, with temporally-varying strengths depending on the ocean wave evolution. Regional properties such as ocean depth and seafloor geometry affect microseism excitation. The shallow ocean depths and uphill slopes around the coast may compose a favorable environment to develop microseism sources. Also, oceanic structures such as plateau, bank, and basin as well as medium properties additionally affect the microseism development. The composite effects of regional environment construct localized stationary microseism sources. Each individual stationary source yields persistent microseism energy flux with consistent azimuthal directionality.

The azimuthal consistency in energy flux from individual microseism sources may allow efficient energy collection using appropriately aligned harvesting devices. We may collect the energy flux from the coherent energy flux that may enable us to accumulate over time. The feature suggests potential utilization of microseisms as a natural energy resource for inaccessible sites where the outer energy supply is naturally limited.

CRediT authorship contribution statement

Seongjun Park: Writing – review & editing, Writing – original draft, Validation, Methodology, Investigation, Formal analysis, Data curation, Conceptualization. **Tae-Kyung Hong:** Writing – review & editing, Writing – original draft, Supervision, Project administration, Methodology, Investigation, Funding acquisition, Conceptualization.

Declaration of competing interest

The authors declare that they have no known competing financial interests or personal relationships that could have appeared to influence the work reported in this paper.

Acknowledgments

We thank Dr. Nidia de Sá Caetano (editor) and two anonymous reviewers for constructive review comments. We are grateful to Deogyong Kim for initial data analysis. The seismic waveforms were collected from the Korea Meteorological Administration (KMA), Korea Institute of Geoscience and Mineral Resources (KIGAM), and National Research Institute for Earth Science and Disaster Resilience (NIED). The hindcast ocean wave model (WAVEWATCH III) was collected from the National Oceanic and Atmospheric Administration (NOAA). This work was supported by the Korea Meteorological Administration Research and Development Program under grant KMI2022-00710. Additionally, this research was partly supported by the Basic Science Research Program of National Research Foundation of Korea (NRF-2017R1A6A1A07015374).

Appendix A. Supplementary data

Supplementary material related to this article can be found online at https://doi.org/10.1016/j.renene.2025.123894.

Data availability

Data will be made available on request.

References

[1] T.K. Hong, I. Kim, S. Park, D. Kil, Elastogravity waves and dynamic ground motions in the Korean peninsula generated by the march 11 2011 M_W 9.0 tohoku-oki megathrust earthquake, J. Geophys. Res.: Solid Earth 126 (e2020JB020628) (2021) http://dx.doi.org/10.1029/2020JB020628.

[2] B. Kim, T.K. Hong, J. Lee, S. Park, J. Lee, Potential seismic hazard in seoul, south korea: a comprehensive analysis of geology, seismic, and geophysical field observations, historical earthquakes, and strong ground motions, Bull. Seism. Soc. Am. 114 (2024) 982–1002, http://dx.doi.org/10.1785/0120230015.

[3] S. Park, T.-K. Hong, H. Buurman, Temporal change of upper-crustal V_P/V_S ratios with volcanic evolution in redoubt volcano, Phys. Earth Planet. Inter. 282 (2018) 39–48, http://dx.doi.org/10.1016/j.pepi.2018.07.003.

[4] T.K. Hong, S. Park, D. Chung, B. Kim, Inversion of acoustic thunder source spectral model from thunder-induced seismic waves in megacity, Geophys. J. Int. 233 (2023) 107–126, http://dx.doi.org/10.1093/gji/ggac440.
[5] T.K. Hong, S. Park, J. Lee, Roles of subway speed and configuration on subway-induced seismic noises in an urban region, J. Appl. Geophys. 202 (2022) 104668, http://dx.doi.org/10.1016/j.jappgeo.2022.104668.
[6] T.K. Hong, J. Lee, G. Lee, J. Lee, S. Park, Correlation between ambient seismic noises and economic growth, Seismol. Res. Lett. 91 (2020) 2343–2354, http://dx.doi.org/10.1785/0220190369.
[7] W. Shen, S. Zhu, H. Zhu, Y.L. Xu, Electromagnetic energy harvesting from structural vibrations during earthquakes, Smart Struct. Syst. 18 (2016) 449–470, http://dx.doi.org/10.12989/sss.2016.18.3.449.
[8] F. Díaz-Mora, A. González-Fallas, Energy harvesting from seismic waves for electricity production, in: E3S Web of Conferences, Vol. 336, 2022, p. 00035, http://dx.doi.org/10.1051/e3sconf/202233600035, EDP Sciences.
[9] Nishida K., Ambient seismic wave field, Proc. Jpn. Acad. Ser. B 93 (2017) 423–448, http://dx.doi.org/10.2183/pjab.93.026.
[10] S. Park, T.-K. Hong, J. Lee, Determination of borehole seismic sensor orientation using microseisms, Bull. Seismol. Soc. Am. 112 (2022) 2327–2343, http://dx.doi.org/10.1785/0120220002.
[11] Longuet-Higgins M.S., A theory of the origin of microseisms, philosophical transactions of the royal society of london, series a., Math. Phys. Sci. 243 (1950) 1–35, http://dx.doi.org/10.1098/rsta.1950.0012.
[12] Hasselmann K., A statistical analysis of the generation of microseisms, Rev. Geophys. 1 (1963) 177–210, http://dx.doi.org/10.1029/GR001i002p00177.
[13] F. Ardhuin, L. Gualtiery, E. Stutzmann, How ocean waves rock the earth: Two mechanisms explain microseisms with periods 3 to 300 s, Geophys. Res. Lett. 42 (2015) 765–772, http://dx.doi.org/10.1002/2014GL062782.
[14] F. Ardhuin, E. Stutzmann, M. Schimmel, A. Mangeney, Ocean wave sources of seismic noise, J. Geophys. Res.: Ocean. 116 (C09004) (2011) http://dx.doi.org/10.1029/2011JC006952.
[15] H.-H. Essen, F. Krüger, T. Dahm, I. Grevemeyer, On the generation of secondary microseisms observed in northern and central europe, J. Geophys. Res. 108 (2506) (2003) http://dx.doi.org/10.1029/2002JB002338.
[16] S. Kedar, M. Longuet-Higgins, F. Webb, N. Graham, R. Clayton, C. Jones, The origin of deep ocean microseisms in the north atlantic ocean. proceedings of the royal society a: mathematical, Math. Phys. Eng. Sci. 464 (2008) 777–793, http://dx.doi.org/10.1098/rspa.2007.0277.
[17] R.A. Haubrich, K. McCamy, Microseisms: Coastal and pelagic sources, Rev. Geophys. 7 (1969) 539–571, http://dx.doi.org/10.1029/RG007i003p00539.
[18] R.C. Aster, D.E. McNamara, P.D. Bromirski, Global trends in extremal microseism intensity, Geophys. Res. Lett. 37 (L14303) (2010) http://dx.doi.org/10.1029/2010GL043472.
[19] P. Gerstoft, P.M. Shearer, N. Harmon, J. Zhang, Global p, PP, PKP Wave Microseisms Obs. from Distant Storms. Geophys. Res. Lett. 35 (L23306) (2008) http://dx.doi.org/10.1029/2008GL036111.
[20] C.T. Tindle, M.J. Murphy, Microseisms and ocean wave measurements, IEEE J. Ocean. Eng. 24 (1999) 112–115, http://dx.doi.org/10.1109/48.740159.
[21] J. Zhang, P. Gerstoft, P.D. Bromirski, Pelagic and coastal sources of p-wave microseisms: Generation under tropical cyclones, Geophys. Res. Lett. 37 (L15301) (2010) http://dx.doi.org/10.1029/2010GL044288.
[22] C. Davy, G. Barruol, F.R. Fontaine, K. Sigloch, E. Stutzmann, Tracking major storms from microseismic and hydroacoustic observations on the seafloor, Geophys. Res. Lett. 41 (2014) 8825–8831, http://dx.doi.org/10.1002/2014GL062319.
[23] Snieder R., Extracting the green's function from the correlation of coda waves: A derivation based on stationary phase, Phys. Rev. E 69 (2004) 046610, http://dx.doi.org/10.1103/PhysRevE.69.046610.
[24] S. Park, T.-K. Hong, Continent-side uplifted mantle and geological imprints along a paleo rift in the western east sea (sea of Japan), J. Geophys. Res.: Solid Earth 129 (2024b) e2024JB029049.
[25] S. Park, T.-K. Hong, Correct off-site determination of seismic sensor orientation from combined analyses of earthquake and microseism records, Bull. Seismol. Soc. Am. 114 (2024a) 942–954, http://dx.doi.org/10.1785/0120230150.
[26] Cessaro R.K., Sources of primary and secondary microseisms, Bull. Seismol. Soc. Am. 84 (1994) 142–148, http://dx.doi.org/10.1785/BSSA0840010142.
[27] S. Chevrot, M. Sylvander, S. Benahmed, C. Ponsolles, J.M. Lefèvre, D. Paradis, Source locations of secondary microseisms in western europe: Evidence for both coastal and pelagic sources, J. Geophys. Res. 112 (B11301) (2007) http://dx.doi.org/10.1029/2007JB005059.
[28] M. Obrebski, F. Ardhuin, E. Stutzmann, M. Schimmel, Detection of microseismic compressional (P) body waves aided by numerical modeling of oceanic noise sources, J. Geophys. Resaerch: Solid Earth 118 (2013) 4312–4324, http://dx.doi.org/10.1002/jgrb.50233.
[29] Z. Wang, F. Niu, J. Huang, Z. Li, H. Chen, Distribution of Rayleigh wave microseisms constrained by multiple seismic arrays, J. Geophys. Res.: Solid Earth 126 (2021) http://dx.doi.org/10.1029/2021JB022084, e2021JB022084.
[30] N.M. Shapiro, M.H. Ritzwoller, G.D. Bensen, Source location of the 26 sec microseism from crosscorrelations of ambient seismic noise, Geophys. Res. Lett. 33 (L18310) (2006) http://dx.doi.org/10.1029/2006GL027010.
[31] A.M. Borzì, V. Minio, F. Cannavò, A. Cavallaro, S. D'Amico, A. Gauci, R.De. Plaen, T. Lecocq, G. Nardone, A. Orasi, M. Picone, A. Cannata, Monitoring extreme meteo-marine events in the mediterranean area using the microseism (medicane apollo case study), Sci. Rep. 12 (2022) 21363, http://dx.doi.org/10.1038/s41598-022-25395-9.
[32] S. Park, T.-K. Hong, Typhoon-induced microseisms around the south China sea, Seismol. Res. Lett. 91 (2020) 3454–3468.
[33] Saito T., Love-wave excitation due to the interaction between a propagating ocean wave and the sea-bottom topography, Geophys. J. Int. 182 (2010) 1515–1523, http://dx.doi.org/10.1111/j.1365-246X.2010.04695.x.
[34] K. Nishida, R. Takagi, Teleseismic s wave microseisms, Science 353 (2016) 919–921, http://dx.doi.org/10.1126/science.aaf7573.
[35] B. Huang, M. Xue, Z. Guo, W. Song, Exploring the deep ocean single-frequency microseisms southwest of Japan in northern philippine sea, in: Geophysical Research Letters, vol. 49, 2022, http://dx.doi.org/10.1029/2021GL097444, e2021GL097444.
[36] J.C. Stachnik, A.F. Sheehan, D.W. Zietlow, Z. Yang, J. Collins, A. Ferris, Determination of new zealand ocean bottom seismometer orientation via Rayleigh-wave polarization, Seismol. Res. Lett. 83 (2012) 704–713, http://dx.doi.org/10.1785/0220110128.
[37] S. Rost, C. Thomas, Array seismology: Methods and applications, Rev. Geophys. 40 (2002) http://dx.doi.org/10.1029/2000RG000100, 2-1-2-27.
[38] J. Schweitzer, J. Fyen, S. Mykkeltveit, S.J. Gibbons, M. Pirli, D. Kühn, T. Kværna, Seismic arrays, in: P. Bormann (Ed.), New Manual of Seismological Observatory Practice 2 (NMSOP-2), Deutsches GeoForschungsZentrum GFZ, Potsdam, Germany, 2012, pp. 1–80, http://dx.doi.org/10.2312/GFZ.NMSOP-2_ch9.
[39] L. Retailleau, P. Bouè, L. Stehly, M. Campillo, Locating microseism sources using spurious arrivals in intercontinental noise correlations, J. Geophys. Res.: Solid Earth 122 (2017) 8107–8120, http://dx.doi.org/10.1002/2017JB014593.
[40] T.J. Sereno, S.R. Bratt, T.C. Bache, Simultaneous inversion of regional wave spectra for attenuation and seismic moment in scandinavia, J. Geophys. Res. 93 (1988) 2019–2035, http://dx.doi.org/10.1029/JB093iB03p02019.
[41] Hong T.-K., Lg attenuation in a region with both continental and oceanic environments, Bull. Seismol. Soc. Am. 100 (2010) 851–858, http://dx.doi.org/10.1785/0120090057.
[42] P.D. Bromirski, F.K. Duennebier, R.A. Stephen, Mid-ocean microseisms, Geochem. Geophys. Geosystems 6 (Q04009) (2005) http://dx.doi.org/10.1029/2004GC000768.
[43] T.-K. Hong, T.S. Kang, Pn travel-time tomography of the paleo-continental-collision and rifting zone around Korea and Japan, Bull. Seismol. Soc. Am. 99 (2009) 416–421, http://dx.doi.org/10.1785/0120080120.
[44] A. Ziv, A.M. Rubin, Static stress transfer and earthquake triggering: No lower threshold in sight? J. Geophys. Res.: Solid Earth 105 (2000) 13631–13642, http://dx.doi.org/10.1029/2000JB900081.
[45] D. Kilb, J. Gomberg, P. Bodin, Triggering of earthquake aftershocks by dynamic stresses, Nature 408 (2000) 570–574, http://dx.doi.org/10.1038/35046046.
[46] X. Mànuel A. Roset, J.Del. Rio, D.M. Toma, N. Carreras, S.S. Panahi, A. Garcia-Benadí, T. Owen, J. Cadena, Ocean bottom seismometer: design and test of a measurement system for marine seismology, Sensors 12 (2012) 3693–3719, http://dx.doi.org/10.3390/s120303693.
[47] D. Carreras N. Moure, S. Gomáriz, D. Mihai, A. Mànuel, R. Ortiz, Design of a smart and wireless seismometer for volcanology monitoring, Measurement 97 (2017) 174–185, http://dx.doi.org/10.1016/j.measurement.2016.11.013.
[48] N. Mohajeri, G. Upadhyay, A. Gudmundsson, D. Assouline, J. Kämpf, J.L. Scartezzini, Effects of urban compactness on solar energy potential, Renew. Energy 93 (2016) 469–482, http://dx.doi.org/10.1016/j.renene.2016.02.053.
[49] E. Kabir, P. Kumar, S. Kumar, A.A. Adelodun, K.H. Kim, Solar energy: Potential and future prospects, Renew. Sustain. Energy Rev. 82 (2018) 894–900, http://dx.doi.org/10.1016/j.rser.2017.09.094.
[50] Celik A.N., A statistical analysis of wind power density based on the Weibull and Rayleigh models at the southern region of Turkey, Renew. Energy 29 (2004) 593–604, http://dx.doi.org/10.1016/j.renene.2003.07.002.
[51] M.R. Islam, S. Mekhilef, R. Saidur, Progress and recent trends of wind energy technology, Renew. Sustain. Energy Rev. 21 (2013) 456–468, http://dx.doi.org/10.1016/j.rser.2013.01.007.